MOCASS: a satellite mission concept using Cold Atom Interferometry for measuring the Earth gravity field

[(*)] Federica Migliaccio[(1)], Mirko Reguzzoni[(1)], Khulan Batsukh[(1)], Guglielmo Maria Tino[(2)], Gabriele Rosi[(3)], Fiodor Sorrentino[(4)], Carla Braitenberg[(5)], Tommaso Pivetta[(5)], Dora Francesca Barbolla[(5)(6)], Simona Zoffoli[(7)]

(*) Corresponding author

(1) Department of Civil and Environmental Engineering, Politecnico di Milano, Italy

(2) Department of Physics and Astronomy and LENS Laboratory, University of Florence, Italy

(3) The National Institute for Nuclear Physics, Florence and AtomSensors srl, Italy

(4) The National Institute for Nuclear Physics, Genova, Italy

(5) Department of Mathematics and Geosciences, University of Trieste, Italy

(6) Department of Science and Technology of Biology and Environment, University of Salento, Lecce, Italy

(7) Italian Space Agency (ASI), Rome, Italy

Abstract

Both GRACE and GOCE have proven to be very successful missions, providing a wealth of data which are exploited for geophysical studies such as climate changes, hydrology, sea level changes, solid Earth phenomena, with benefits for society and the whole world population. It is indispensable to continue monitoring gravity and its changes from space, so much so that a GRACE follow-on mission has been launched in 2018.

In this paper a new satellite mission concept named MOCASS is presented, which can be considered as a GOCE follow-on, based on an innovative gradiometer exploiting ultra-cold atom technology and aimed at monitoring Earth mass distribution and its variations in time. The technical aspects regarding the payload will be described, illustrating the measurement principle and the technological characteristics of a Cold Atom Interferometer that can measure gravity gradients. The results of numerical simulations will be presented for a one-arm and a two-arm gradiometer and for different orbit configurations, showing that an improvement with respect to GOCE could be obtained in the estimate of the static gravity field over all the harmonic spectrum (with an expected error of the order of 1 mGal at degree 300 for a 5-year-mission) and that estimates are promising also for the time-variable gravity field (although GRACE is still performing better at very low degrees). Finally, the progress achievable by exploiting MOCASS observations for the detection and monitoring of geophysical phenomena will be discussed: the results of simulations of key geophysical themes (such as mass changes due to hydrology, glaciers and tectonic effects) with expected gravity change-rates, time constants and corresponding wavelengths, show that an improvement is attainable and that signals invisible to past satellites could be detected by exploiting the Cold Atom technology.

Keywords: Earth's gravity field; Cold Atom Interferometry; Satellite gradiometry; Geophysical phenomena; Mass distribution; Spherical harmonics.

1. Introduction: future missions for the gravity field

The purpose of this Section is to highlight the need for an on-going monitoring of the Earth's gravity field, providing also a brief overview of recently launched or proposed mission concepts.

Indeed, GRACE and GOCE have proved to be very successful missions, providing a wealth of data which have been exploited for studying climate changes, hydrology, sea level changes, solid Earth phenomena. It appears that also in the future it will be indispensable to monitor gravity and its changes from space.

The GRACE mission (Tapley and Reigber 2001) was launched in 2002; it has measured changes in the Earth's gravity field, exploiting low-low satellite-to-satellite tracking (SST) using microwave K/Ka-band ranging and high-low SST using GPS. GRACE Follow-On was launched in 2018 (Flechtner et al., 2014), (Kornfeld et al., 2019). The mission re-flies a pair of similar spacecraft and instruments, with changes intended to improve the mission performance; besides, it is also testing an advanced laser instrument to improve the accuracy of inter-spacecraft ranging (low-low SST) by tenfold or more and lead to enhanced gravity measurements. The Next Generation Gravity Mission (NGGM), proposed by the European Space Agency, is also focused on the use of this laser technology (Cesare et al. 2016), designing a mission based on two couples of GRACE-like satellites (Bender et al. 2009). More complex satellite formations have been also proposed, such as the mass variation observing system by high low inter-satellite links (MOBILE), again exploiting the laser technology for the measurement of the distances between satellites at different orbital altitudes (Pail et al. 2019).

The GOCE satellite (Drinkwater et al. 2003) was launched in 2009 and the mission lasted until the end of 2013; it exploited high-low SST using GPS and an on-board electrostatic gravity gradiometer. Future improvements in the GOCE mission concept can only be achieved by going beyond the technology of electrostatic gradiometers, taking advantage of a new generation of sensors. In fact, a new and highly improved gradiometer concept has been proposed (Carraz et al. 2014) exploiting instruments that have been refined and tested over nearly three decades, based on the principle of Cold Atom Interferometry (CAI). Such instruments operate as inertial sensors and have been used for fundamental physics experiments (Rosi et al. 2014). Based on this principle, a gradiometer in one given direction (e.g. the radial one) can be obtained by measuring the differential acceleration of two clouds of ultra-cold atoms separated by a distance of e.g. 50 cm.

The same instrument can provide a simultaneous measurement of the rotation angle around a given axis. In addition, this scheme can be repeated in the three directions to have all diagonal elements of the gravity gradient tensor and the angular rate vector.

Thus, it will be possible to exploit atom interferometry for inertial and gravity sensing payloads. It has been proved that a flat noise power spectral density can be assumed also at low frequency (Sorrentino et al. 2014), thus avoiding the

spectrally colored noise of the electrostatic accelerometers in the lower frequencies**.** In this sense the use of such an instrument allows to address the requirements of a mission dedicated to both the static gravity field (Douch et al. 2018), like GOCE, and the time variable gravity field, like GRACE. Of course, in the latter case a longer lifetime is required and this reflects in a proper mission profile.

The geophysical impact of a future mission with significantly improved performances with respect to GRACE and GOCE has been deeply studied in recent years, see e.g. Panet et al. (2013) and Gruber et al. (2014). In particular, a very important initiative was carried out under the umbrella of the International Union of Geodesy and Geophysics (Pail et al. 2015a, b) with the aim to determine the science and user needs for a future satellite gravity observing system for a variety of applications, so that the identified requirements shall be addressed by future mission studies. Most of the concepts proposed are somehow based on a future GRACE-like mission, possibly with more complex satellite configurations but still based on the principle of the low-low SST. The simulated data analysis and mainly the geophysical implications of a future GOCE-like mission, i.e. based on the satellite gradiometry concept, are less investigated by the scientific community and are the subject of this work.

2. Gravity gradient measurement with ultra-cold atom interferometry

In this Section, the mathematical principles of an innovative payload represented by an ultra-cold atom interferometer for the measurement of the gradients of the Earth gravity potential will be presented, alongside a discussion on the sensitivity of this instrument.

2.1 Measurement principle

Matter-wave interferometry, i.e. the observation of quantum interference of De Broglie waves, provides extremely sensitive and accurate sensors for the measurement of inertial forces, with important implications both in fundamental physics and in applied research. Atom interferometers are especially suited for precision measurements, as the atomic wave-packets can be manipulated by means of laser fields (Tino and Kasevich 2014). Light-pulse interferometry is largely applied in metrology and gravitational physics, where it provides precise measurements of gravity acceleration (Kasevich and Chu 1992), Earth's gravity gradient and rotations. Experiments based on atom interferometry include tests of the Einstein's Equivalence Principle, measurement of fundamental constants, tests of general relativity and Newton's $1/r^2$ law, and search of quantum gravity effects. Atom interferometry gravitational waves detectors have also been proposed. Mobile accelerometers based on atom interferometry have been developed for many practical applications including metrology, geodesy, geophysics, prospecting for oil or minerals and inertial navigation.

In light-pulse atom interferometry, the atoms are left in free fall and optical pulses are used to stimulate Raman or Bragg transitions between two different quantum states during free fall. The use of two-photon transitions with counter-propagating laser fields allows to impart the significant momentum of optical photons to the atom, with a precise control of relative phases in the radio-frequency domain. These light pulses act on the atom matter-waves in the same way as mirrors and beam splitters act on the light-wave in an optical interferometer. If the initial population is in one single internal state, a $\pi/2$ Raman pulse produces a 50% splitting into the two states with a momentum difference, giving a spatial separation and thus acting as a 50% beam-splitter; a π Raman pulse reverses the atomic population and produces a momentum change, thus acting as a mirror. A simple Mach-Zehnder interferometer is obtained with a $\pi/2$-π-$\pi/2$ sequence of three equidistant pulses. It can be shown that if such a pulse sequence is applied with a wave-vector parallel to the mean atomic velocity, the resulting phase difference accumulated along the atom interferometer paths is given by

$$\Delta\varphi = k_{eff}\ a\,T^2 \qquad [2.1]$$

where a is the acceleration of the atoms along the wave-vector of lasers, T is the temporal separation between two interferometer pulses (interaction time) and k_{eff} is the effective wave-vector of the Raman transition

$$k_{eff} = k_2 + k_1 \cong -2k_1 \qquad [2.2]$$

where k_1 and k_2 represent the wave-vectors of the two counter-propagating optical photons. The scale factor of the quantum sensor is thus given by the space-time area $k_{eff}T^2$ between the two atomic trajectories, which is proportional to the product of the momentum difference provided by the Raman splitter and the square of the temporal separation between the splitting laser pulses. The sequence of three Raman pulses as described above provides a single measurement of the gravity acceleration. Repeating the sequence improves the statistical uncertainty with the square root of the repetition rate, since the different measurements are averaged incoherently.

An atom interferometry measurement of the gravity gradient is based on the simultaneous acceleration measurement with two spatially separated atomic clouds in free fall. By using the same atom optics tool to manipulate the atomic wave-packet of the two atomic clouds, effects that are common to both clouds cancel out when computing the differential acceleration, which implies that common noise sources, e.g. vibrations of the mirror, are suppressed to a very large extent.

The sensitivity of current ground-based atom interferometry gravity gradiometers reaches a few tens of E/√Hz (Sorrentino et al. 2014), and it is ultimately limited by shot noise in the number of detected atoms. One major limitation of ground-based light-pulse atom interferometry sensors is the short interaction time achieved due to the free fall of atoms in a 1-g environment. An improvement of several orders of magnitude is expected in a microgravity environment, since the sensitivity scales as the square of the interaction time. An additional improvement is obtained by replacing the simple Raman splitters with sequences of light pulses imparting multiple photon recoils, in order to increase the separation between atomic trajectories.

Application of CAI sensors has been investigated both theoretically and experimentally, see for instance (Tino et al. 2013). Similarly to the case of the GOCE gradiometer, residual fluctuations of the differential Cold Atom Interferometer phase will pose requirements on environmental parameters. However, drag control would be less critical with the Cold Atom gradiometer than in GOCE, due to the better matching in scale factor. Moreover, the atoms only interact with the environment through the laser wave-fronts during Raman pulses. This allows to control several sources of de-coherence and systematic errors, as will be discussed below in this section. In addition, a dual-cloud Cold Atom gradiometer can measure acceleration and gravity gradient at the same time (Sorrentino et al. 2012). On the other hand, the Cold Atom gradiometer will be sensitive to fluctuations in the magnetic field via the second-order Zeeman effect.

Space implementation of a gravity gradiometer in nadir-pointing configuration requires the simultaneous knowledge of the rotation rate in order to subtract the centrifugal acceleration from the data. With a suitable configuration, the Cold Atom sensor can measure one component of the gravity gradient and the rotation rate along a transverse axis at the same time. This can be realized with two pairs of atom clouds in free fall (Carraz et al. 2014); in each pair, the two atom clouds are launched with opposite velocities; the two pairs of clouds are spatially separated along a direction orthogonal to their velocities (the sensitive axis for gravity measurement). The setup can be properly scaled to a multi-axial configuration. To exploit the advantage of microgravity environment, it is convenient to increase the duration of the single interferometric sequence up to the point where the sensitivity starts to be limited by the residual thermal expansion of the ultra-cold atom clouds. To gain statistical sensitivity, the measurement repetition rate can be increased by interleaving several atom interferometers (Dutta et al. 2016). The maximum repetition rate is limited by the preparation time of the ultra-cold atom clouds and by the cross-talk between interleaved measurements. In the following we will assume an inter-pulse separation $T = 5$ s and a repetition rate of 1 Hz as in (Carraz et al. 2014).

As will be discussed in Section 2.2, operating an atom interferometer in a rotating frame requires to counter-rotate the Raman wave-vector to compensate for the Coriolis acceleration (Lan et al. 2012). This is not compatible with the simultaneous operation of atom interferometers on counter-propagating atom clouds, which is required for rotation rate

measurements. In the following we will thus consider a simplified setup (**Fig. 1 a**) with a single pair of atom clouds propagating in the same direction.

Using separate interaction regions for the three Raman pulses allows a passive, static counter-rotation of the laser wave-vector (**Fig. 1 b**) to compensate the average value of the satellite rotation rate, and so to manage the large angular dynamic range ($\Omega_{orb}T \approx 7$ mrad) required for rotation compensation. Small residual rotation errors can be compensated by active tip-tilt actuation on the last retro-reflection mirror.

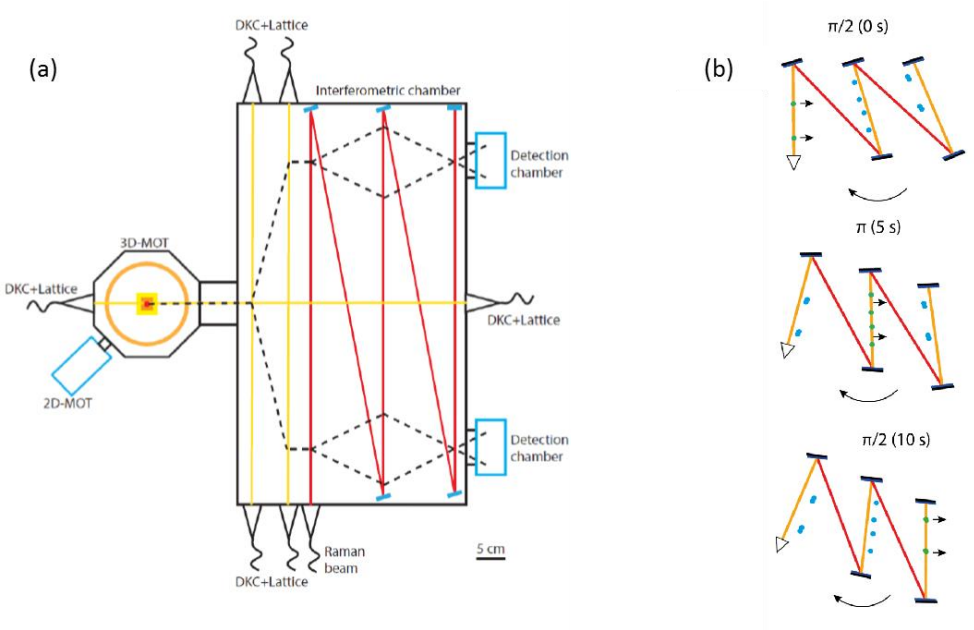

Fig. 1

(a) The CAI space gradiometer payload: solid black lines indicate the mechanical structure of the vacuum chamber and fiber-optic collimators; dashed black lines indicate the trajectories of atom clouds; yellow lines indicate laser beams for delta-kick cooling (DKC) and optical lattices providing precise momentum kicks to the atoms; red lines indicate Raman laser beams for the atom interferometry splitters

(b) Static compensation for spacecraft rotation in order to cancel Coriolis acceleration: mirrors are aligned to form an angle $\Omega_{orb}T$ between the Raman wave-vectors at successive pulses

The space Cold Atom gradiometer requires atom clouds at nanoKelvin temperatures. These can obtained with standard laser cooling methods: atoms are trapped and cooled to micro-Kelvin temperatures in a separate vacuum chamber using a three-dimensional magneto-optical trap (3D-MOT), loaded from an high-flux atomic source such as a 2D-MOT. After release from the trap, the atoms are further cooled to a Bose-Einstein condensate (BEC) at nanoKelvin temperature with delta-kick cooling (Kovachy et al. 2015), and sent to the main vacuum chamber with a velocity of $v \approx 25$ mm/s using an optical lattice to impart several photon recoils in a direction orthogonal to the gradiometer sensitive axis. In the main chamber the atoms are illuminated with a sequence of two optical lattice pulses along the gradiometer sensitive axis, to

split the atoms in two clouds with a separation of $d \approx 50$ cm. The two atomic clouds are simultaneously illuminated with Raman light pulses to implement the interferometric sequence, and are finally detected with fluorescence imaging.
The main components of a Cold Atom gradiometer, i.e. laser system, physics package and control electronics, have already reached sufficient technology readiness level for operation in microgravity. Proof-of-principle atom interferometry experiments are being performed, with different technological solutions, on parabolic flights (Geiger et al. 2011) and on sounding rockets (Becker et al. 2018). The laser system for cooling, trapping and Raman transitions is based on fiber optic components qualified for telecom standards (Telecordia) in parabolic flights experiments, and on micro-integrated optics components in sounding rocket experiments.

2.2 Sensitivity of the Cold Atom gradiometer

The ultimate sensitivity to gravity gradient can be limited by either instrumental or environmental effects. While the former are similar as in ground experiments, the space environment poses stringent requirements to the control of dynamic effects on the Cold Atom sensor.
A full derivation of the atom interferometer response is beyond the scope of this paper. Here we describe the basic features, referring to references for further details. The output phase of an atom interferometer can be calculated with a semi-classical formalism for Lagrangians that are second order in position and velocity (Hogan et al. 2009). In the case of quadratic Hamiltonians, and for a three-pulse Mach-Zehnder interferometry in double diffraction configuration, the phase of the atom interferometer can be expressed as

$$\varphi = 2k_{eff} r_{A1} - 4k_{eff} \frac{r_{A2} + r_{B2}}{2} + 2k_{eff} \frac{r_{A3} + r_{B3}}{2} \qquad [2.3]$$

where r_{ij} is the position of the atom along the path i ($i = A, B$) at the j-th Raman pulse ($j = 1, 2, 3$). In this study, the atomic trajectories have been calculated for two dynamical configurations of the satellite, i.e. nadir-pointing and inertial-pointing modes (see Section 3.1).
To describe the nadir-pointing mode we use the Lagrangian

$$L = \frac{1}{2} m \left[\mathbf{v} + \mathbf{\Omega} \times (\mathbf{r} + \mathbf{R})\right]^2 + m\,\mathbf{g} \cdot \mathbf{r} + \frac{1}{2} m\,\mathbf{r}\,\Gamma\,\mathbf{r} \qquad [2.4]$$

where *m* is the mass of the atom, $\vec{v}$ and $\vec{r}$ the velocity and position of the atom in the satellite frame, $\vec{R}$ the position of the satellite from the Earth center, $\vec{\Omega}$ the angular velocity of the satellite around the Earth, and Γ the gravity gradient tensor. We choose a reference frame aligned with the spacecraft main axes; therefore, in the nadir pointing configuration the *x*, *y* and *z* axis are pointing approximately in the along-track, cross-track and radial direction, respectively.

In the following we specify the case of a radial Cold Atom gradiometer: the sensitive axis, i.e. the direction of the Raman wave-vector as well as the separation of the two atomic clouds, is approximately along *z*, and the launch velocity of the atom clouds is along the *x* axis. If the Raman beam is counter-rotated at an angular rate $\sim -\vec{\Omega}$, the atom interferometer phase depends on the residual rotation rate $\overrightarrow{\delta\Omega}$ of the optical wave-vector. For simplicity we only consider a non-vanishing component $\delta\Omega_y$ of the residual rotation along *y*, which gives the major contribution. Under these assumptions the gradiometer phase from Equations [2.3] and [2.4] is

$$\Phi = 2k_{eff}T^2T_{zz}\,d + k_{eff}T^2T_{zz}(\delta z + \delta v_z T) + 2k_{eff}T^2\,d\,\delta\Omega_y^2 + 4k_{eff}T^2\delta v_x\delta\Omega_y^2 \qquad [2.5]$$

Here *d* is the interferometer baseline, i.e. the distance between the two atom clouds, T_{zz} is the diagonal component in the *z* direction of the gravity gradient tensor, while δz and δv_i indicate errors on the differential position and velocity of the two atom clouds. The first term of Equation [2.5] represents the gradiometer readout signal, the following terms are the main error contributions due to local gradient, centrifugal acceleration and Coriolis acceleration.

In particular the second and fourth phase terms depend on the coupling of gravity gradient and angular velocity components with the components of atomic differential positions and velocities. Such terms produce both errors in the gradient measurement, due to non-vanishing mean values of the differential position and/or velocities of the atomic clouds, and a loss of contrast in the atom interferometer due to the finite temperature of the atoms. The centrifugal acceleration term produces errors in the gradient measurement.

The Coriolis and centrifugal terms are largely mitigated with counter-rotation of the Raman wave-vector across the interferometric sequence (Lan et al. 2012). The noise term due to local gradient can be efficiently mitigated with a suitable chirp of the Raman laser frequency during the interferometric sequence (Roura 2017).

If we now consider the inertial-pointing mode, to describe it we use the Lagrangian

$$L = \frac{1}{2}m\left[\mathbf{v} + \mathbf{\Omega}\times(\mathbf{r}+\mathbf{R})\right]^2 + \frac{1}{2}m\,\mathbf{r}\,R(\Omega_{orb})\Gamma R^T(\Omega_{orb})\,\mathbf{r} \qquad [2.6]$$

where the matrix $R(\Omega_{orb})$ describes the rotation of the gravity gradient tensor around the *y* axis. Under the above mentioned assumptions, the atom gradiometer phase is again given by Equation [2.5], where T_{zz} is modulated by the orbital rotation around *y*.

The effect of time dependent perturbations on the atom interferometer is conveniently modelled with the formalism of the sensitivity function (Cheinet et al. 2008).

In the case of stationary, zero-mean disturbances (i.e. random vibrations), the noise sources are properly described by a Power Spectral Density (PSD) $S_n(f)$; the resulting RMS phase noise of the atom interferometer is calculated as

$$\sigma_\varphi^2 = \int_0^\infty S_n(f)\left|H_n(f)\right|^2 df \qquad [2.7]$$

where $H_n(f)$ is the atom interferometer transfer function from the disturbance to the atom interferometry phase.

The response of the atom interferometer to a time varying gravity gradient $\gamma(t)$ along the direction of the Raman wave-vector, such as the field observed from an instrument in orbit, can be calculated similarly to the acceleration noise by considering that $\gamma(t) = \Delta a(t)/d$. The phase variation of the differential interferometer due to temporal changes of the gravity gradient can be expressed as

$$\delta\varphi_\gamma = k_{eff}\, T^2 d \int_{-\infty}^{\infty} h(t)\,\gamma(t)\,dt \qquad [2.8]$$

where *h(t)* is the phase impulse response function of the atom interferometer (also called "CAI integrator" in the following), and is shown **Fig. 2**. The corresponding frequency-domain transfer function from gravity gradient to interferometer phase is given by

$$H_\gamma(f) = k_{eff} T^2 d\, H(f) = -\frac{4k_{eff} T^2 d\,\Omega^2}{\Omega^2 - (2\pi f)^2} \frac{\sin(\pi f T)}{(2\pi f T)^2} \left\{ \sin\left[\pi f (T - 2\tau)\right] + \frac{2\pi f}{\Omega} \cos(\pi f T) \right\} \qquad [2.9]$$

where *H(f)* is the Fourier transform of *h(t)* (also shown in **Fig. 2**), τ is the duration of Raman pulses, and Ω is the so-called "Rabi frequency" of the Raman transition (Foot 2004).

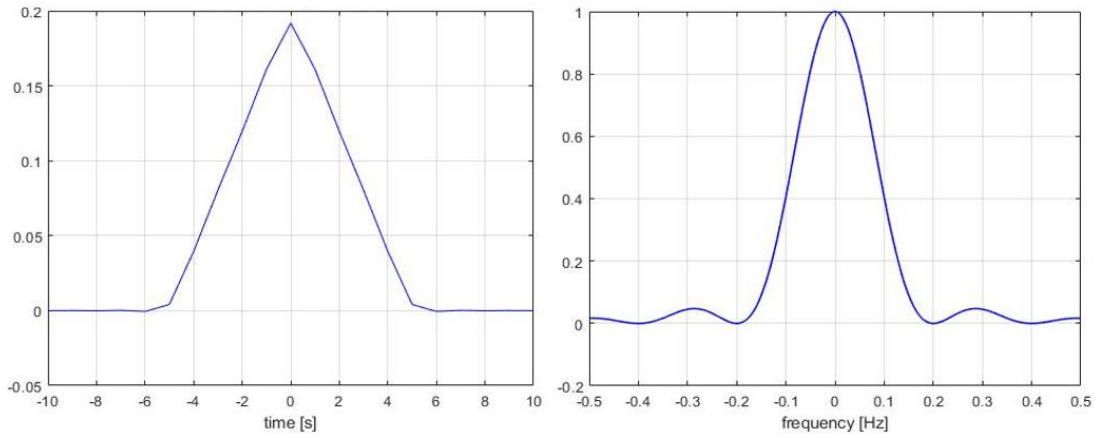

Fig. 2

The CAI response function *h(t)* in the time domain (left) and the corresponding Fourier transform *H(f)* in the frequency domain (right)

A fundamental limit to the sensitivity of the CAI gradiometer is given by the Quantum Projection Noise, which scales as the inverse square root of the number N of detected atoms times the repetition rate T_r, and produces an equivalent PSD of the gravity gradient noise ν, which is

$$S_\nu(f) = \frac{2T_r}{N}\frac{1}{H_\gamma^2(f)} \approx \frac{2T_r}{N}\left(\frac{1}{k_{eff}T^2 d}\right)^2 \qquad [2.10]$$

The ASD (Amplitude Spectral Density) of the gravity gradient noise for the CAI interferometer including the main noise terms described above is shown in **Fig. 3** in the case of nadir-pointing and radial (z) sensitive axis, assuming fluctuations of 10 μm/s RMS for the residual velocity difference between atom clouds, a typical GOCE-like orbit and a compensation of the rotation rate at the level of 10^{-8} rad/s.

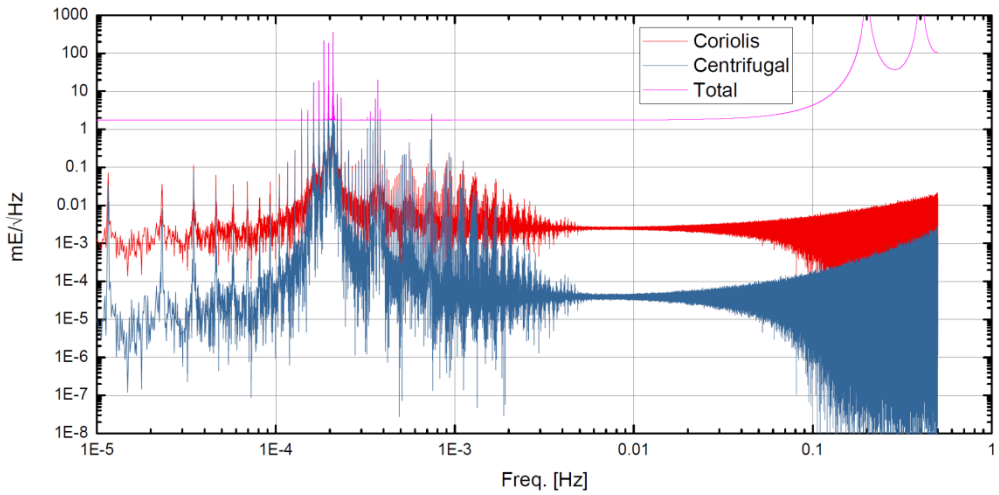

Fig. 3

The ASD of the gravity gradient noise with dominant terms (nadir-pointing mode)

3. Numerical simulations and data analysis

To explore and quantify the advantages which MOCASS could provide with respect to previous gravity missions, several simulations have been carried out and the data have been analyzed by means of the so-called "space-wise" approach. In this Section the rationale of the MOCASS data simulations will be described, taking into account the characteristics of the cold-atom interferometer and its performances (namely, its error PSD). Besides, the "space-wise" procedure applied to the data analysis will be presented, with the results obtained for several different mission scenarios based on different satellite orbit altitudes, operation modes and gradiometer configurations.

3.1 Rationale of the MOCASS data simulations

The data were simulated considering a cold-atom interferometer in two different configurations: (i) a single-arm gradiometer measuring the gradient of the potential in one direction, this being the along-track direction (T_{xx} data) or the out-of-plane direction (T_{yy} data) or the radial direction (T_{zz} data); (ii) a double-arm gradiometer measuring the gradients of the potential in two directions, these being the T_{xx} and T_{zz} components, or the T_{yy} and T_{zz} components.

Summarizing, the rationale of the MOCASS simulations were the following:

- for the payload, the outcome from the computations of the Cold Atom interferometer sensitivity in the different possible configurations have been used in the form of error PSD, in order to simulate observations which could represent measurements in the most realistic way, see Fig. 3;
- for the orbit data, the parameters of the GOCE orbit have been applied regarding altitude and inclination of the mission, namely almost-circular sun-synchronous orbit at two different altitudes: "high" (H_{sat} ~ 259 km) and "low" (H_{sat} ~ 239 km); note that in principle a polar orbit would be desirable, in order to cover also polar areas with measurements, however it is more realistic to consider a sun-synchronous mission; the time span of the simulation is two months, in order to have a dense enough spatial data coverage; the static gravity field is sampled from the EIGEN_6C4 global model perturbed according to its error degree variances, while the time-variable gravity field is not modelled in the simulated data;
- two possible pointing modes have been considered: the nadir-pointing mode and the inertial one; in the former, the Z axis is radially oriented, the Y axis is perpendicular to the orbital plane and the X axis is almost tangential completing the right-hand triad; in the latter, the X axis is orthogonal to the equator at the Greenwich meridian, the Y axis is tangential to the equator at the Greenwich meridian and the Z axis is parallel to the Earth rotation axis; of course it is understood that the inertial pointing mode at such low altitude would be extremely challenging from a space system engineering point of view.

3.2 The space-wise approach for the analysis of MOCASS data

The simulated data were analyzed by exploiting the so-called "space-wise approach", originally studied and implemented at Politecnico di Milano. The main idea behind the space-wise approach is to estimate the spherical harmonic coefficients of the geopotential model by exploiting the spatial correlation of the Earth gravity field. For this purpose, a collocation solution can be devised, modelling the signal covariance as a function of spatial distance, but not of time distance, as it is done for the noise covariance. In this way, data that are close in space but far in time can be filtered together, thus overcoming the problems related to the strong time correlation of the observation noise.
Since a unique collocation solution is computationally unfeasible due to the huge amount of data of a gravity mission, the space-wise approach requires to be implemented as a multi-step collocation procedure (Migliaccio et al. 2004; Reguzzoni and Tselfes 2009), basically consisting of (i) a Wiener filtering and deconvolution (Papoulis 1984; Reguzzoni 2003) along the orbit to reduce the highly time correlated noise of the gradiometer and to account for the Cold Atom gradiometer transfer function, (ii) a spherical grid interpolation at mean satellite altitude by applying collocation on local patches of data (Migliaccio et al. 2007), (iii) a spherical harmonic (SH) analysis by numerical

integration (Colombo 1981) to derive the geopotential coefficients. A simplified scheme of the space-wise approach and simulation procedure is shown in **Fig. 4**.

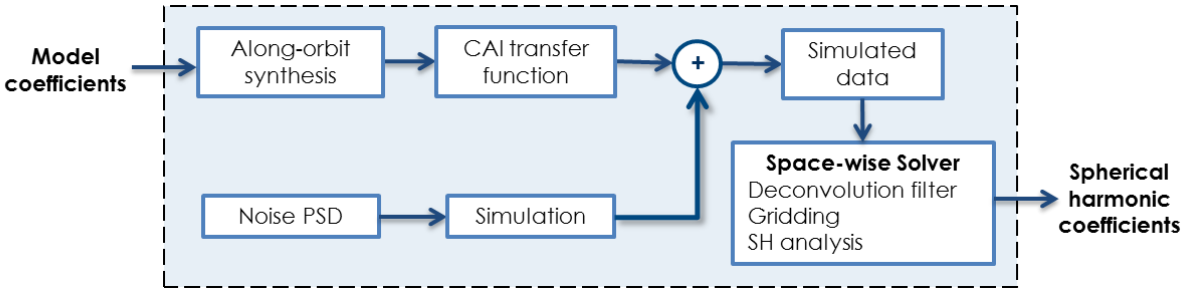

Fig. 4
Simplified flow chart of the space-wise approach and simulation procedure

The basic assumption is that we have a flow of data consisting of the gravity signal and the measurement noise, which are both stationary processes (with own covariances), but independent from one another. The observation equation in the time domain can be written as:

$$y_0(t) = h(t) * y(t) + v(t) \qquad [3.1]$$

where $y_0(t)$ is the vector of the observations; $h(t)$ is the transfer function of the CAI instrument (CAI integrator); $y(t)$ is the signal and $v(t)$ is the measurement error. The star operator stands for the time convolution.
According to the Wiener-Kolmogorov theory, the optimal estimate of the signal along the orbit is given by the following deconvolution filter:

$$W(f) = \frac{H(f) S_y(f)}{H^2(f) S_y(f) + S_v(f)} \qquad [3.2]$$

where $H(f)$ is the (real) Fourier transform of the CAI integrator (see again **Fig. 3**); $S_y(f)$ is the PSD of the signal; $S_v(f)$ is the PSD of the noise.
In **Fig. 5** (left panel) the noise ASD of the MOCASS ultra-cold atom gradiometer can be seen and compared with the corresponding ASD of the measurement error of the GOCE gradiometer: the MOCASS gradiometer clearly shows high values only at high frequencies, while the GOCE gradiometer shows high values at both low and high frequencies. The ultra-cold atom gradiometer noise PSD parameters are: interaction time T = 5 s, repetition rate T_r = 1 s, number of

atoms $N = 10^6$, distance $d = 50$ cm. In **Fig. 5** (right panel), the shape of the Wiener deconvolution applied to the simulated MOCASS data is shown and compared with the Wiener filter for the GOCE data. Note the small amplification at the high frequency cutoff, due to the deconvolution operation on the MOCASS data; since GOCE data could be considered as point-wise observations, the deconvolution operation was not required in that case.

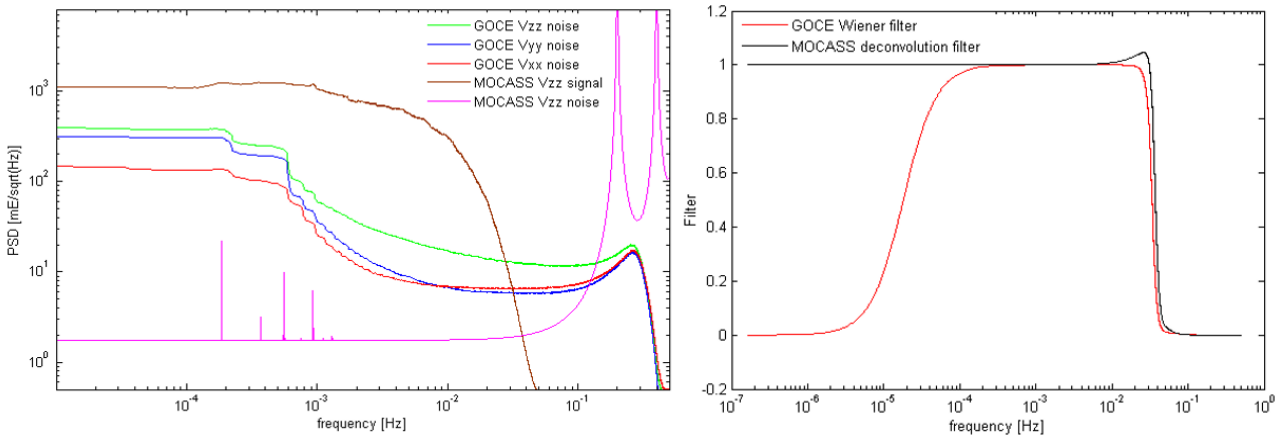

Fig. 5

On the left: noise ASD of the MOCASS Cold Atom gradiometer compared with the corresponding ASD of the measurement error of the GOCE gradiometer; on the right: GOCE Wiener filter (red curve) vs. MOCASS Wiener deconvolution filter (black curve)

Another important aspect in the space-wise approach is the gridding procedure. In the MOCASS simulations, T_{xx}, T_{yy} and T_{zz} observations were considered to predict grids of T, T_{rr} and $T_{\lambda\lambda}$ values. These functionals of the anomalous potential were chosen because they are easy to analyze in spherical harmonics by numerical integration. The gridding was performed by means of a local collocation, using a suitable method for data selection, which is fundamental to ensure the good quality of the results. Basically, an "ensemble" of observation points was selected for each grid knot, the ensemble having a decreasing spatial density with an increasing distance from the grid knot. Furthermore, the signal covariance was locally adapted by using scale factors calibrated with respect to the reference model used for the data simulation (Reguzzoni et al. 2014).

The observation equation at epoch t, corresponding at the position in space with spherical coordinates (ϑ , λ , r), being ϑ the colatitude, λ the longitude and r the radius, is given by:

$$\hat{y}_0(\vartheta,\lambda,r)_t = y(\vartheta,\lambda,r)_t + e(t) \qquad [3.3]$$

where *e(t)* is the Wiener deconvolution estimation error. Defining $\hat{\mathbf{y}}_0$ as the vector of observations falling in the "ensemble" of a grid knot $P(\vartheta, \lambda)$ and $r = R$ the radius of the boundary sphere, the local collocation gridding is written as:

$$\hat{z}(\vartheta,\lambda) = \mathbf{C}_{yz}^{T}(C_{yy} + C_{ee})^{-1}\,\hat{\mathbf{y}}_0 + \eta(\vartheta,\lambda) \qquad [3.4]$$

where $\hat{z}(\vartheta,\lambda)$ is the functional (T, T_{rr} or $T_{\lambda\lambda}$) predicted at the grid knot P and η is the corresponding prediction error; $\mathbf{C}_{yz}$ is the cross-covariance vector between the observed functionals in the point "ensemble" and the predicted functional at the grid knot P; C_{yy} is the covariance matrix of the observed functionals; C_{ee} is the covariance matrix of the Wiener deconvolution estimation error. Correlations between observed functional and Wiener deconvolution estimation error are here neglected.

The harmonic analysis for the estimation of the geopotential coefficients was performed by numerical integration, based on the well-known quadrature equations (Heiskanen and Moritz, 1967) which hold on the boundary sphere Σ:

$$\hat{T}_{\ell m} = \frac{1}{4\pi\, a_{\ell m}} \int_{\Sigma} \hat{z}(\vartheta,\lambda)\, Y_{\ell m}(\vartheta,\lambda)\, d\sigma \approx \frac{1}{4\pi a} \sum_{i,j} \hat{z}(\vartheta_i,\lambda_j)\, Y_{\ell m}(\vartheta_i,\lambda_j)\, \Delta\sigma_{ij} \qquad [3.5]$$

where $T_{\ell m}$ are the spherical harmonic coefficients expressed as integrals of spherical harmonic functions $Y_{\ell m}$. Besides, the parameter $a_{\ell m}$ represents a function of degree ℓ and order m, depending on the functional z of the anomalous potential predicted on the boundary sphere, and $\Delta\sigma_{ij}$ represents the area of the cell of the grid at latitude ϑ_i and longitude λ_j.

In order to calculate the estimation errors (grid and coefficient errors), Monte Carlo samples of spherical harmonic coefficients $T_{\ell m}^{k}$ (k = 1, 2, …, N) were drawn from a reference model, then observations along the orbit were consistently simulated and the space-wise approach was applied to these simulated data, obtaining samples of estimated grid values $\hat{z}^{k}$ and of estimated coefficients $\hat{T}_{\ell m}^{k}$ (Migliaccio et al. 2009). The sample error RMS were thus computed as:

$$\hat{\sigma}_z(\vartheta,\lambda)=\sqrt{\frac{1}{N}\sum_{k=1}^{N}\left[\hat{z}^k(\vartheta,\lambda)-z^k(\vartheta,\lambda)\right]^2} \qquad [3.6]$$

$$\hat{\sigma}_{\ell m}=\sqrt{\frac{1}{N}\sum_{k=1}^{N}(\hat{T}^k_{\ell m}-T^k_{\ell m})^2} \qquad \forall\,\ell,m \qquad [3.7]$$

3.3 Results for the gravity field estimation

For the MOCASS study numerical simulation activity, several different scenarios were implemented based on different satellite orbit altitude, operation mode and gradiometer configurations.

The statistics of the results of the numerical simulations were computed exploiting a Monte Carlo (MC) approach, using the coefficients variances of the reference model EIGEN_6C4 (Förste et al. 2014) to generate 20 MC samples of spherical harmonic coefficients.

Table 1 shows the error RMS of the predicted grid of T_{rr} values for the case of both a single-arm gradiometer and a double-arm gradiometer, depending on the observed data from which the grids were predicted. These results show that the optimal scenarios are represented by grids predicted from T_{yy} in the inertial pointing mode or T_{zz} in the nadir pointing mode in the case of a single-arm gradiometer. In the case of a double-arm gradiometer the best results are obviously obtained by grids predicted combining observations of T_{yy} and T_{zz} regardless of the pointing mode. Note that in the double-arm gradiometer, the available cold atoms are split into two directions, and this is why the overall accuracy is not improved.

Table 1

Error RMS of the predicted grid of T_{rr} values for the case of a single-arm gradiometer and a double-arm gradiometer; statistics are computed by excluding polar gap latitudes; the time span of the input data is two months

Pointing mode	**Orbit**	**Error RMS of predicted T_{rr} values [mE]**				
		T_{xx}	T_{yy}	T_{zz}	T_{xx} **and** T_{zz}	T_{yy} **and** T_{zz}
Nadir pointing mode	High orbit (~ 259 km)	1.22	1.76	0.36	0.56	0.55
	Low orbit (~ 239 km)	0.92	1.29	0.22	0.30	0.34
Inertial pointing mode	High orbit (~ 259 km)	4.52	0.45	2.91	0.76	0.55
	Low orbit (~ 239 km)	1.49	0.33	2.77	0.40	0.34

An analysis of the behavior of the grid error RMS along parallels has also shown that in the latitude range which excludes the polar gaps due to the satellite orbit inclination, the error in the optimal cases for a single-arm (T_{yy} in inertial

pointing mode, T_{zz} in nadir pointing mode) and for a double-arm gradiometer (T_{yy} and T_{zz} in both inertial and nadir pointing modes) remains below the level of 0.6 mE.

Considering the "optimal" cases reported in **Table 1**, the results were found to be very similar for the high orbit or low orbit cases and for the inertial or nadir pointing modes. Therefore only some examples will be reported in the following.

Fig. 6 shows the error degree variances for MOCASS in terms of reconstruction of a global gravity model for a two-month mission in high orbit with a single-arm gradiometer in the case of T_{zz} observations (nadir-pointing mode) or T_{yy} observations (inertial-pointing mode). The curves are compared with the corresponding curves for the GRACE and GOCE error degree variances and show the improved behavior of the MOCASS results, apart from the low frequency spherical harmonics (say, up to degree 40), where GRACE results remain superior. In the case of GOCE, formal error degree variances of the time-wise R1 solution (Pail et al. 2011) that is based on about two months of data are plotted In the case of GRACE, the monthly solutions of November and December 2009 are averaged to get a model consistent with the GOCE time-wise R1 solution. All error curves are plotted disregarding low order coefficients affected by polar gap degradation (Sneeuw and van Gelderen 1997).

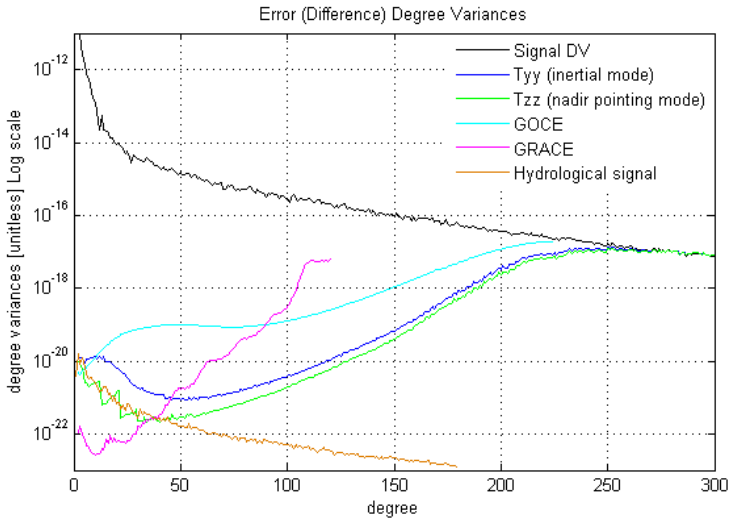

Fig. 6

Error degree variances in terms of reconstruction of a global gravity model for a 2-month MOCASS mission in high orbit and observations of a single-arm gradiometer; as a comparison, 2-month GOCE and GRACE solutions are represented, as well as the degree variances of the static gravity signal and the hydrology signal, as generated within the ESA-project "ESA Earth System Model for Gravity Mission Simulation Studies" (Dobslaw et al. 2015)

Of course, if the aim is to obtain a static gravity field model, the quality of the solution improves by exploiting a much longer observation period, at least of the duration of 1 year. As an example, **Fig. 7** (left panel) shows the expected

improvement in the estimation of Δg at ground level for different mission periods, going from 1-year observations to 2-year observations to 5-year observations, considering T_{zz} data in nadir-pointing mode in high orbit.

On the other hand, the level of accuracy attainable by MOCASS in estimating the time variable gravity signals is represented in **Fig. 7** (right panel), which shows the cumulative errors in estimating a linear trend of gravity anomalies, with monthly solutions, for a 1-year, 2-year and 5-year mission, again considering T_{zz} data in nadir-pointing mode in high orbit.

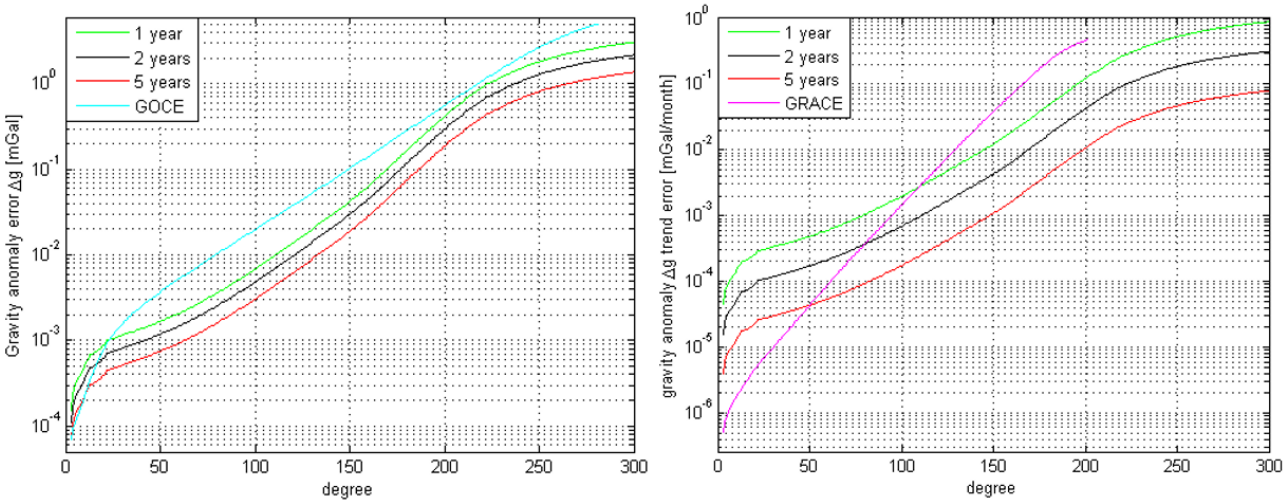

Fig. 7

On the left: cumulative error in terms of gravity anomaly Δg at ground level for a presumed duration of the MOCASS mission equal to 1, 2 or 5 years and the one of GOCE for the complete mission period; on the right: trend estimation cumulative error for the gravity anomaly Δg at ground level, using one-month solutions of the MOCASS mission over a period of 1, 2 or 5 years and the one of GRACE (5-year-mission with one-month-solutions); in both cases T_{zz} observations have been considered in nadir-pointing mode and high orbit

Summarizing, by applying the space-wise approach to the analysis of simulated MOCASS observations (including orbital filtering modification due to the Cold Atom gradiometer "integration") the following results were obtained:

- for the static gravity field: an improvement with respect to GOCE performances was seen over all the harmonic spectrum (error of ~ 1.4 mGal at degree 300, ~ 0.9 mGal at degree 250 for a 5-year-mission);
- for the time-variable gravity field: the MOCASS error estimates are promising (the two-month solution is better than the GRACE one already above degree 40, while in the case of GOCE this occurs above degree 90). However, the accuracy at very low degrees seems to be still insufficient for this type of applications.

4. Detection and monitoring geophysical phenomena by exploiting MOCASS observations

In this Section the impact of MOCASS will be presented, comparing the estimation of wavelengths and amplitudes of geophysical phenomena of interest with MOCASS error curves, showing that an improvement occurs in the detection of signals invisible to past satellites. In other words, the percentage of observable phenomena should be significantly higher than with previous missions.

The approach used is an extension of the assessment that had been made in Pail et al (2015a,b) relative to a NGGM satellite mission. In the former study the signals of hydrology, glaciers, earthquakes and mantle signals were estimated at ground level, and the amplitudes and possibly emerging wavelengths of the phenomena compared with the error spectral curves. Here a similar approach is performed, but calculating the expected fields at satellite height and only assessing the wavelength of major amplitude of a signal. In particular, we assess in which cases MOCASS bears an improvement in the detection of signals invisible to past satellites. In other words, given a number-size distribution of the phenomena (e.g. a database of glaciers), the percentage of observable phenomena should be significantly higher than with previous missions, in order to give a significant improvement in the detection. The term "number-size distribution" is equivalent to the statistical distribution of the number of occurrences of a phenomenon as a function of its size, and it is quantified by the histogram of the occurrences of the sizes. In the case of glaciers we intend the histogram of the areas recovered from a database of glaciers, in the case of seamounts the histogram would display the distribution of the volume of seamounts.

The High Mountains of Asia (HMA) region, defined as the Himalaya range and Tibetan plateau, has been used as testing area because it includes huge hydrologic movements, a tectonic activity and a wide glacierized area that has been subjected to prevalent melting in recent years (Gardner et al. 2013). Simulations of seamount growth in oceans have been considered too. All gravity simulations are calculated using tesseroids (Uieda et al. 2016) or a numerical solution of the Poisson equation through a finite element solver.

4.1 Yearly ice thickness variations in HMA

We constrain the yearly deglaciation mass variations in HMA through the RGI Randolph Glacier Inventory (Pfeffer et al. 2014) and a map of yearly ice thickness variations (Gardner et al. 2013). The RGI offers outlines of glaciers and it is derived from satellite imagery data; we considered all glaciers of the HMA region, covering an area of 100,000 km^2. The ice thickness variations of Gardner et al. (2013) are based on ICESat data for the period 2003-2009 and rates were calculated for 11 different macro-regions defined in the RGI catalogue. They are shown as green lines in **Fig. 8**. A general decrease of the ice thickness is found for the whole region, with an average rate of -0.34 m/yr ± 0.29 m/yr and a

maximum deglaciation rate of -0.89 m/yr ± 0.18 m/yr in the Eastern Himalaya. The glaciers were discretized with tesseroids of sides 0.02° × 0.02°, bottom placed on topography, and top corresponding to the yearly mass loss. The ice-density was assumed to be constant and equal to 900 kg/m^3. The gravity field was calculated at the satellite height of 250 km.

The yearly gravity change rate and the outlines of the 11 glacierized areas calculated at 250 km height (units mGal/yr) are shown in **Fig. 8**. A negative arch like shape trend up to 4 10^{-4} mGal/yr is seen, along the northern, western and southern border of Tibet.

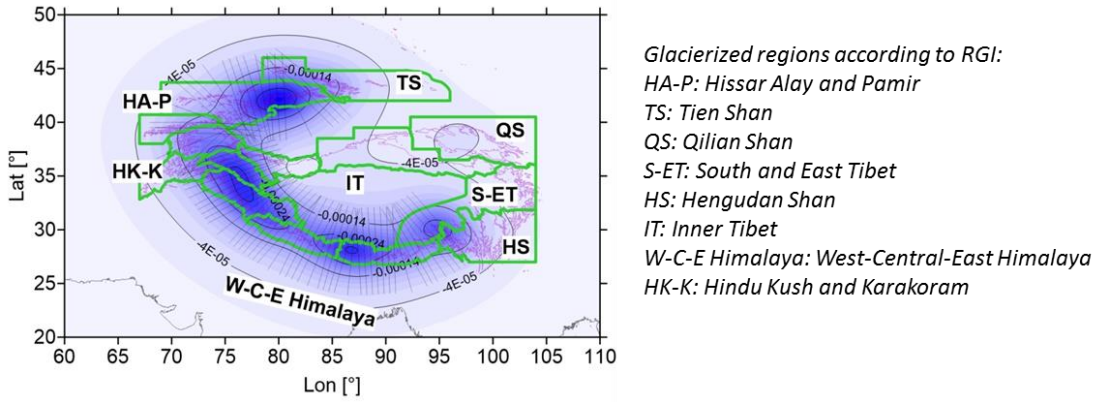

Fig. 8

Simulated deglaciation gravity change rates in HMA calculated at 250 km height in mGal/yr; grey lines are the profile traces used for the analysis of the signals (see Section 3.2); green lines are the borders of the regions with homogenous deglaciation rate; purple marks the 3500 m height contour line; coastline in grey; isolines are gravity change rates in mGal/yr

4.2 Tectonic vertical movements and hydrology

Vertical topographic movements recorded by GNSS imply a mass change, since uplifting topography replaces air with rock. Additional mass changes are located at the crust-mantle transition, where an uplift produces a mass surplus due to mantle replacing crust. Amplitudes of change rates have been estimated to be of the order of 10^{-4} mGal/yr and wavelengths of several hundred km in Tibet and Alps (Braitenberg and Shum 2017; Chen et al. 2018; Yi et al. 2016). A similar analysis was conducted in Tibet, constraining the vertical movement with over 500 GNSS vertical rates (Liang et al. 2013; Fu and Freymueller 2012). The GNSS time-series, shown in **Fig. 9** with black (subsidence) and green (uplift) dots, show a complex deformation pattern. A broad crustal rise is observed in the Himalaya, Southern Tibet and the Qilian Shan regions but uplift rate is non-uniform. The maximum uplift is observed in the peripheral areas, with vertical movements of over 5 mm/yr; Tibet is uplifting at a lower rate (< 2 mm/yr). Local subsidence of

1-2 mm/yr is observed in the Lhasa terrane, in the Tarim basin and in the south-eastern portions of the Qilian Shan. The mass change is modelled by interpolating the uplift rates on a regular grid of 0.25°.

Simulated yearly gravity changes due to superficial hydrology are also shown in **Fig. 9**. The hydrological variations in the HMA region were estimated through the GLDAS model (Rodell et al. 2004), which offers the integrated moisture mass of the first 2 m of the soil. The GLDAS product has been already successfully employed to predict and remove the hydrological effects on different geodetic time-series such as GRACE gravity time series or GNSS data, with applications also in the HMA (Matsuo and Heki 2010; Yi et al. 2016).

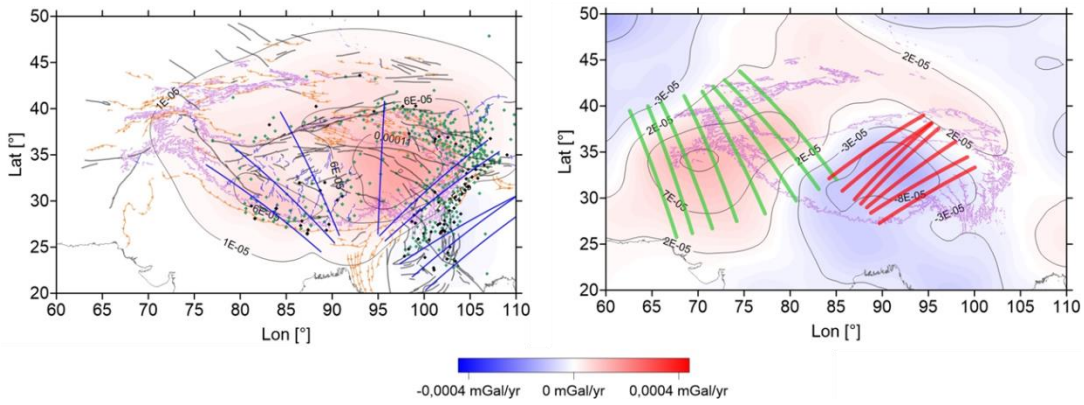

Fig. 9

Simulated gravity changes in HMA due to tectonic uplift (left) and long period hydrology (right); green dots are GNSS stations recording uplift, black subsidence; orange lines: main thrust systems; black and blue lines: strike-slip and normal faults; long blue, green and red lines are the profile traces on which the characteristic amplitude and wavelength of the signals are estimated; purple marks the 3500 m height contour line; coastline in grey

For our purpose, we rely on the monthly GLDAS model with 0.25° spatial resolution. For each grid cell, the long period linear trend of the time-series was estimated. The GLDAS model accounts only for superficial hydrologic mass variations, which in many cases is the dominant effect because the most important water level variations occur in the phreatic systems. However, long period trends could show mass variations due to pauperisation of deeper aquifers systems, but a database with the time-series of water level wells was not available.

The mass changes were discretized with tesseroids and the gravity was calculated at 250 km height. For tectonic effects crustal and mantle density are 2670 and 3200 kg/m^3, respectively. The tectonic gravity change is dominated by a positive rate in Eastern Tibet; the hydrologic signal has a negative signature with two separate lobes in the South Eastern Tibet and in the lowlands below the western Himalaya syntax. All amplitudes are below 10^{-4} mGal/yr.

4.3 Seamount growth

Monitoring the submerged seamounts growth, anticipating a hazard to ships, is of wide interest and is presently a challenge, since other techniques such as GNSS cannot be exploited. We tested the sensitivity of MOCASS to a seamount growth during an episodic eruption. The eruption should be a non-explosive magma outflow of basaltic lava at the top, which is immediately cooled by the ocean, analogous to the formation of pillow lavas. We choose a seamount with a cone-like shape with radius 12500 m, height above seafloor 5800 m, top at 200 m below sea surface (Wessel et al. 2010). We successively add magmatic volume to the top, with an increasing height from 5 m up to 150 m. Our model does not include the dynamic model of the magmatic production of a seamount, so we suppose that the feeder channel from lower crust and mantle continuously supplies the magma chamber. In the case that the magma chamber outpours the magma, but is not refilled from below, the mass change would be smaller.

4.4 Impact of MOCASS: time variable phenomena

The simulated gravity is analyzed along profiles crossing prominent anomalies. An estimation of signal amplitude and wavelength is obtained by fitting a Gaussian function to the profiles. The dispersion of the Gaussian function is set equal to 1/4 of the wavelength λ, and the amplitude is taken as the double signal magnitude. These criteria reflect the Gaussian function representing one full wavelength of a sinusoidal function. The wavelength λ (in degrees) is converted to the spherical harmonic degree of the spectrum through $n=360/\lambda$.

The typical amplitude-wavelength estimates for the time varying phenomena are shown in **Fig. 10**; for each phenomenon we report the average wavelength, amplitude and the standard deviation.

Red and green dots report the gravity signal generated by long period hydrologic trends, black dots tectonic signals, blue dots the ice thickness variations and grey triangles seamount growth. The solid lines refer to error curves after 1-year mission, the dashed lines report the errors of monthly solutions. Compared to **Fig. 6**, here the error degree variances are given in terms of gravity anomalies at a satellite altitude of 250 km.

Comparing GRACE and MOCASS curves, we observe that MOCASS shows a flatter error curve at degrees higher than 40. This could lead to an improvement in the detection of crustal movements. The black dot labelled NT indicates a localized tectonic signal in the North Tibet, which is currently only observable by MOCASS mission. Exploiting MOCASS, with 2-year models, we expect to get a clearer picture of the underground mass movements.

The hydrologic long period trends show signal amplitudes slightly higher with respect to tectonic effects; GRACE is already able to resolve most of the signals, while MOCASS, with the flat error curve for degree $\ell > 40$, detects some high frequency signals that are below the GRACE curve. These high frequency signals are located in central Tibet,

where several small hydrologic basins are present. In this case MOCASS shows its complementarity with GRACE mission in the hydrologic characterization.

As shown in **Fig. 10**, the seamounts growth produces the highest amplitudes in our simulations. The eruption signals are compared with monthly solutions since an eruptive event could last from few days up to several months. The numbers indicate the height variation of the seamount. MOCASS is able to recover a less than 10 m increase in the height of the seamount, while GRACE would need an increase of more than 5 m. In terms of erupted volumes, 5 m height increase is equivalent to $8.2 \cdot 10^8$ m^3, while 10 m generates a volume of $1.6 \cdot 10^9$ m^3, similar to the Saint Helens eruption of 1980.

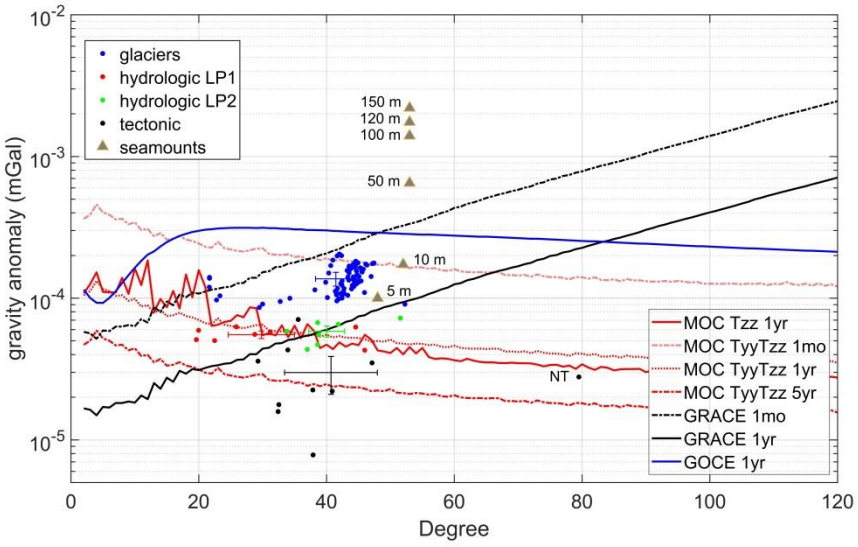

Fig. 10

Spectral comparison of the simulated gravity change for each of the geophysical phenomena with the error curves of satellites GRACE, GOCE and MOCASS in two configurations; error curves after 1 month, 1 year or 5 years of observations; MOC Tzz: MOCASS nadir-pointing single-arm configuration; MOC Tyy Tzz: MOCASS nadir-pointing double-arm configuration; GRACE and GOCE curves are computed by rescaling formal errors of the whole mission solutions down to one year and one month; each data point corresponds to the signal amplitude estimated along one profile crossing the High Mountain of Asia in Fig. 9; the numbers indicate the height variation of the seamount; NT is the tectonic signal in Northern Tibet

Melting glaciers are responsible for signals with wavelengths of 8-9° (ℓ = 40 - 45) and amplitudes up to $2 \cdot 10^{-4}$ mGal/year. Considering 1-year sampling, GRACE and MOCASS are both able to detect these gravity changes, MOCASS however can easily sense smaller deglaciation rates. If the deglaciation rates in the HMA would lower to half the actual value, GRACE would not be able to detect this mass loss. This quality improvement in the observations of the deglaciation phenomena could contribute in better defining the yearly mass variations in the HMA (Matsuo and Heki 2010; Jacob et al. 2012). To demonstrate this, we analyse the sensitivity of MOCASS to detect ice mass variations

as a function of the glacierized area extent. Each area is subjected to three different deglaciation rates, then the simulated fields have been analysed. **Fig. 11** reports the signal amplitude as a function of glacier area and rate of deglaciation.

We found that glacier areas smaller than 500 km^2 are below resolution of the satellites. Starting with an area of 1900 km^2, the deglaciation can be observed, for rates above 0.89 m/yr, but only with MOCASS, not with GRACE. The same rate could be seen by GRACE considering an area as big as 4750 km^2, while also smaller rates (-0.4 m/yr) are detected by MOCASS.

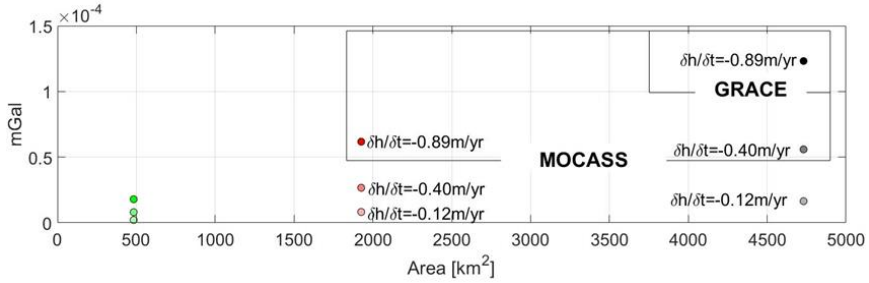

Fig. 11

Gravity change in one year versus area of glaciers for different height losses of the glaciers; the individual simulations are compared to the error curves in the upper graph

4.5 Glacier static signal detectability

In order to further prove the MOCASS mission quality we considered the problem of total mass detection of a glacier. These static simulations are of interest for exploration purposes: if we know the glaciers surface area from satellite imagery, we could use MOCASS measurements to estimate the thickness. To construct the synthetic models we exploited the RGI catalogue and extracted five glaciers outlines in the HMA region with different sizes. Then given the area A of the glacier, we estimated the volume V using the empirical formula (Bahr et al. 2015): $V=0.03A^{1.36}$

From volume and area we estimate an average glacier thickness and calculated the gravity effect at 10 km height assuming a density contrast against rocks of $|\Delta\rho|=1600$ kg/m^3.

Considering the statistical distribution of the number of glaciers versus size, as shown in **Fig. 12**, MOCASS achieves a significant step ahead, because at sizes around 100 km^2 the number of smaller glaciers significantly jumps with respect to larger glaciers from 20% to 60%. With smaller areas, close to 100 km^2 the number of glaciers is 20 fold, which demonstrates that MOCASS achieves a very significant increase in glacier monitoring, because it crosses the border between copious and scarce number of glaciers, at least for the HMA.

The estimate of detectable glaciers was exclusively based on the comparison of the expected signal and the instrumental noise level: the problem of signal separation was not considered. The measured gravity field will be the sum of all mass

change effects (Gruber et al. 2011; Dobslaw et al. 2015), and the separation of the glacier mass requires to reduce the effects of sediments and crustal density inhomogeneity (static case) and effects of mass changes from atmosphere, hydrology and solid-Earth mass change phenomena for the dynamic case. The error on signal separation depends on the amount of knowledge of the other contributors, which is variable from place to place. The tectonic mass changes are only present in tectonically active areas, and are irrelevant over tectonically stable lithosphere. For areas in which seismic investigations have been carried out and which are well surveyed, the sediment thickness and densities may be well known, and can be reduced from the signal. But areas which have never been surveyed and for which neither the glacier thickness nor the thickness of the sediment cover is known, the separation of these two signals in the gravity field will be affected by larger error and uncertainties.

Due to the large variability of situations, the estimation of the sensitivity of the satellite to the single phenomena is here performed by comparing the signal of the single sources to the error curve of the satellite payload. If the estimated signal is above the noise threshold, it will be detectable in the observed field. The signal separation of the different sources is a totally different problem and it is at the core of the research of the scientific users of the mission data. The signal separation is beyond the scope of the study, which is only to assess the signals which are above the instrumental noise-level.

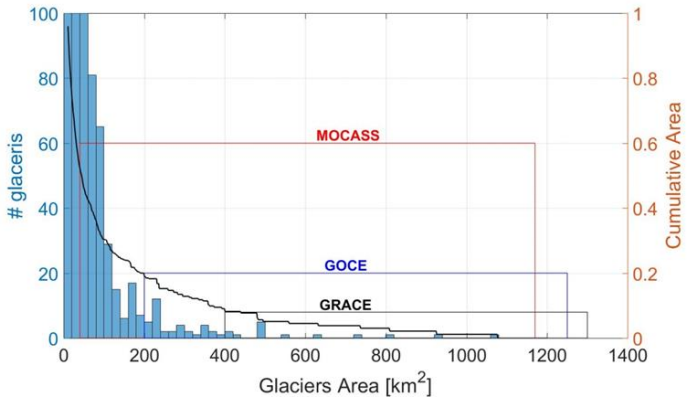

Fig. 12

Statistical distribution of number of glaciers in HMA with respect to their size; boxes show the detectability ranges of the three satellites GRACE, GOCE and MOCASS; the first bin reaches the value of 1600; the second about 750; the third about 200; the black line gives the fraction of total cumulative glaciered area for glaciers larger than a given glacier size

5. Conclusions

During the MOCASS study an innovative mission concept has been devised, based on advanced Cold Atom interferometry accelerometers representing the payload of a spacecraft flying in a low orbit around the Earth, with the aim to acquire observations of the Earth gravity field with accuracy and spatial resolution surpassing those already achieved with previously successful missions. The goal is to compute gravity models allowing to monitor with high resolution mass variations which occur on and below the Earth surface, thus gaining a better insight in a variety of geophysical phenomena.

During the MOCASS study, different aspects were taken into account, in particular:

- the instrumental aspects of a Cold Atom interferometer were studied and defined for this particular type of mission, in terms of long term stability, accuracy, and spectral characteristics;
- simulations of the observations were performed, based on the instrumental characteristics of the Cold Atom interferometer, and solutions were computed in terms of Earth gravity models, to define the resolution and accuracy which could be attained;
- key geophysical themes were simulated, modelling mass changes due to hydrology, glaciers and tectonic effects, to investigate the expected gravity change-rates, time constants and wavelengths at satellite and ground level.

Technological applications of Cold Atom sensors are strictly related to the ability of such instruments to characterize with high accuracy and stability the full gravity gradient tensor. The outcome of this project has been the design of an instrument capable of simultaneously measuring the gravity acceleration and the gravity gradient in satellite operation. The critical aspects of the Cold Atom interferometer have also been taken into account, in particular those depending on the different satellite orbit configuration (inertial and nadir), proposing mitigation strategies to address them. The sensitivity of the interferometer has been evaluated through the use of a proper transfer function (the Fourier transformation of the sensitivity function) and subsequent computation of the PSD of the instrument. However, it has to be noted that the satellite-instrument coupling errors have been neglected in this study, implying more optimistic estimates of the gravity gradient noise PSD, especially in the *x* and *z* directions.

To explore and quantify the advantages that MOCASS could provide with respect to previous gravity missions, during the study several simulations have been carried out and the data have been analyzed by means of the so-called "space-wise" approach. The data were simulated either for the case of a single-arm gradiometer (T_{xx}, T_{yy}, T_{zz} components) or for the case of a double-arm gradiometer (T_{xx} and T_{zz} components, T_{yy} and T_{zz} components). The results showed that regarding the recovery of the static gravity field, the MOCASS error estimates are lower than those of GOCE over all the harmonic spectrum, especially at high degrees, with a commission error of about of 1.4 mGal at degree 300, 0.9

mGal at degree 250 and 0.19 mGal at degree 200 for a 5-year mission in nadir pointing mode, using a single-arm gradiometer in radial direction. For the case of the time-varying gravity field, the MOCASS error estimates are promising since the two-month solution is better than the GRACE one above degree 40. It has to be stressed that flying a mission in nadir or inertial pointing mode at such a low altitude, including the required attitude control, is very challenging from the engineering point of view.

A fundamental part of the MOCASS study was to evaluate the significance of the mission for the improvement in the detection and monitoring of geophysical phenomena, estimating the progress that could be achieved. To answer this question, realistic simulations of different phenomena were set up. The simulations regarded deglaciation in High Mountain of Asia (HMA); mountain building processes (tectonic); continental hydrology; volcanic eruptions leading to growing seamounts. Regarding the detection of mass distribution, the results showed that MOCASS observations could increase the detectability of small trends in the glacier ice mass in the HMA region and improve the studies of seamounts. Regarding the monitoring of mass variations in time, the simulations showed that MOCASS could detect smaller areas subject to deglaciation in HMA (with respect to GRACE); complex tectonic deformation in the HMA could be mapped with higher resolution; seamounts accretion detectability could be improved (volcanic eruptions at sea), although the applicability in the sense of early warning would remain a challenge, since sufficient integration time is needed to recover the small gravity signal that is produced this phenomenon.

Acknowledgments

The MOCASS study has been funded under ASI contract N. 2016-9-U-0 “Proposal of a satellite mission and sensor concept based on advanced atom interferometry accelerometers for high resolution monitoring of mass variations on and below the Earth surface”.

References

Bahr DB, Pfeffer WT, Kaser G (2015) A review of volume-area scaling of glaciers, Reviews of Geophysics, 53, 95–140, DOI: 10.1002/2014RG000470.

Becker D, Lachmann MD, Seidel ST et al (2018) Space-borne Bose–Einstein condensation for precision interferometry, Nature, 562, 391–395, DOI: 10.1038/s41586-018-0605-1.

Bender PL, Wiese DN, Nerem RS (2009) A possible dual-GRACE mission with 90 and 63 inclination orbits. In: Proc. of the 3rd International Symposium on Formation Flying, Missions and Technologies, Noordwijk (NL), April 2008.

Braitenberg C, Shum CK (2017) Geodynamic implications of temporal gravity changes over Tibetan Plateau. Italian Journal of Geosciences, 1361, 39–49, DOI: 10.3301/IJG.2015.38.

Carraz O, Siemes C, Massotti L, Haagmans R, Silvestrin P (2014). A spaceborne gravity gradiometer concept based on cold atom interferometers for measuring Earth's gravity field, Microgravity Science and Technology, 26, 139–145, DOI: 10.1007/s12217-014-9385-x.

Cesare S, Allasio A, Anselmi A, Dionisio S, Mottini S, Parisch M, Massotti L, Silvestrin P (2016) The European way to gravimetry: From GOCE to NGGM, Advances in Space Research, 57(4), 1047–1064, DOI: 10.1016/j.asr.2015.12.012.

Cheinet P, Canuel B, Pereira Dos Santos F, Gauguet A, Yver-Leduc F, Landragin A (2008) Measurement of the Sensitivity Function in a Time-Domain Atomic Interferometer, IEEE Transactions on Instrumentation and Measurement, 57(6), 1141–1148, DOI: 10.1109/TIM.2007.915148.

Chen W, Braitenberg C, Serpelloni E (2018) Interference of tectonic signals in subsurface hydrologic monitoring through gravity and GPS due to mountain building, Global and Planetary Change, 167, 148–159, DOI: 10.1016/j.gloplacha.2018.05.003.

Colombo OL (1981) Numerical methods for harmonic analysis on the sphere. Report No. 310, Department of Geodetic Science and Surveying, The Ohio State University, Columbus, Ohio.

Dobslaw H, Bergmann-Wolf I, Dill R, Forootan E, Klemann V, Kusche J, Sasgen I (2015). The updated ESA Earth System Model for future gravity mission simulation studies. Journal of Geodesy, 89(5), 505–513. https://doi.org/10.1007/s00190-014-0787-8

Douch K, Wu H, Schubert C, Müller J, Pereira Dos Santos F (2018) Simulation-based evaluation of a cold atom interferometry gradiometer concept for gravity field recovery. Advances in Space Research, 61(5), 1307–1323, DOI: 10.1016/j.asr.2017.12.005.

Drinkwater MR, Floberghagen R, Haagmans R, Muzi D, Popescu A (2003) GOCE: ESA's first Earth Explorer Core Mission. In: Beutler G., Drinkwater M.R., Rummel R., Von Steiger R. (eds), Earth gravity field from space - from sensors to Earth science, Space Sciences Series of ISSI, 17, 419–432, Springer, Dordrecht.

Dutta I, Savoie D, Fang B, Venon B, Garrido Alzar CL, Geiger R, Landragin A (2016) Continuous Cold-Atom Inertial Sensor with 1 nrad/sec Rotation Stability, Physical Review Letters, 116(18), 183003, DOI: 10.1103/PhysRevLett.116.183003.

Flechtner F, Morton P, Watkins M, Webb F (2014) Status of the GRACE Follow-on Mission, in Marti U. (Ed.), Gravity, Geoid and Height Systems: Proc. of the IAG Symposium GGHS2012, 9 - 12 October 2012, Venice, Italy, (IAG Symposia; 141).

Förste C, Bruinsma SL, Abrikosov O, Lemoine J-M, Marty JC, Flechtner F, Balmino G, Barthelmes F, Biancale R (2014) EIGEN-6C4 The latest combined global gravity field model including GOCE data up to degree and order 2190 of GFZ Potsdam and GRGS Toulouse. GFZ Data Services, DOI: 10.5880/icgem.2015.1.

Foot CJ (2004) Atomic Physics, Oxford University Press, Oxford.

Fu Y, Freymueller JT (2012) Seasonal and long-term vertical deformation in the Nepal Himalaya constrained by GPS and GRACE measurements, Journal of Geophysical Research: Solid Earth, 117, B03407, DOI: 10.1029/2011JB008925.

Gardner AS, Moholdt G, Cogley JG, Wouters B, Arendt AA, Wahr J, Berthier E, Hock R, Pfeffer WT, Kaser G, Ligtenberg SRM, Bolch T, Sharp MJ, Hagen JO, van den Broeke MR, Paul F (2013) A Reconciled Estimate of Glacier Contributions to Sea Level Rise: 2003 to 2009. Science, 340, 852–857, DOI: 10.1126/science.1234532.

Geiger R, Menoret V, Stern G, Zahzam N. Cheinet P, Battelier B, Villing A, Moron F, Lours M, Bidel Y et al. (2011) Detecting inertial effects with airborne matter-wave interferometry, Nature Communications, 2, 474, DOI: 10.1038/ncomms1479.

Gruber T, Bamber JL, Bierkens MFP, Dobslaw H, Murböck M, Thomas M, van Beek LPH, van Dam T, Vermeersen A, Visser PNAM (2011) Simulation of the time-variable gravity field by means of coupled geophysical models. Earth System Science Data, 3(1), 19–35. https://doi.org/10.5194/essd-3-19-2011

Gruber T, Murböck M, NGGM-D Team (2014) e2.motion - Earth System Mass Transport Mission (Square) - Concept for a Next Generation Gravity Field Mission. Final Report of Project "Satellite Gravimetry of the Next Generation (NGGM-D)", Deutsche Geodätische Kommission der Bayerischen Akademie der Wissenschaften, Series B, vol. 2014, no. 318, C.H. Beck, ISBN (Print) 978-3-7696-8597-8, http:// dgk.badw.de/fileadmin/docs/b-318.pdf

Heiskanen WA and Moritz H (1967) *Physical Geodesy*, W.H. Freeman and Company.

Hogan JM, Johnson DMS and Kasevich MA (2009) Light-pulse atom interferometry, in: Atom Optics and Space Physics, Proc. of the International School of Physics "Enrico Fermi", course168, Edited by E. Arimondo, W. Ertmer, W. P. Schleich and E. Rasel, IOS Press Amsterdam, Washington, DC, pp. 411.

Jacob T, Wahr J, Pfeffer WT, Swenson S (2012) Recent contributions of glaciers and ice caps to sea level rise. Nature, 482, 514–518. DOI: 10.1038/nature10847.

Kasevich M, Chu S (1992) Measurement of the gravitational acceleration of an atom with a light-pulse atom interferometer, Applied Physics B, 54(5), 321–332, DOI: 10.1007/BF00325375.

Kornfeld RP, Arnold BW, Gross MA, Dahya NT, Klipstein WK, Gath PF, Bettadpur S (2019) GRACE-FO: the Gravity Recovery and Climate Experiment Follow-On Mission, Journal of Spacecraft and Rockets, DOI: 10.2514/1.A34326

Kovachy T, Hogan JM, Sugarbaker A, Dickerson SM, Donnelly CA, Overstreet C, Kasevich MA (2015) Matter wave lensing to picokelvin temperatures, Physical Review Letters, 114, 143004, DOI: 10.1103/PhysRevLett.114.143004.

Lan SY, Kuan PC, Estey B, Haslinger P, Mueller H (2012) Influence of the Coriolis Force in Atom Interferometry, Physical Review Letters, 108, 090402.

Liang S, Gan W, Shen C, Xiao G, Liu J, Chen W, Ding X, Zhou D (2013) Three-dimensional velocity field of present-day crustal motion of the Tibetan Plateau derived from GPS measurements. Journal of Geophysical Research. 118, 5722–5732, DOI: 10.1002/2013JB01050.

Matsuo K, Heki K (2010) Time-variable ice loss in Asian high mountains from satellite gravimetry. Earth and Planetary Science Letters, 290, 30–36, DOI: 10.1016/j.epsl.2009.11.053.

Migliaccio F, Reguzzoni M, Sansò F (2004) Space-wise approach to satellite gravity field determination in the presence of coloured noise. Journal of Geodesy, 78(4-5), 304–313. DOI: 10.1007/s00190-004-0396-z.

Migliaccio F, Reguzzoni M, Sansò F, Tselfes N.(2007) On the use of gridded data to estimate potential coefficients. Proceedings 3rd GOCE User Workshop, Frascati, ESRIN, November 2006, ESA SP-627, European Space Agency, Noordwijk, 311–318.

Migliaccio F, Reguzzoni M, Sansò F, Tselfes N (2009) An Error Model for the GOCE Space-Wise Solution by Monte Carlo Methods. In: Sideris M.G. (eds) Observing our Changing Earth. International Association of Geodesy Symposia, vol. 133. Springer, Berlin, Heidelberg.

Pail R, Bruinsma S, Migliaccio F, Förste C, Goiginger H, Schuh WD, Höck E, Reguzzoni M, Brockmann JM, Abrikosov O, Veicherts M, Fecher T, Mayrhofer R, Krasbutter I, Sansò F, Tscherning CC (2011) First GOCE gravity field models derived by three different approaches. Journal of Geodesy, 85, 819–843, DOI: 10.1007/s00190-011-0467-x.

Pail R Ed. (2015a) Observing Mass Transport to Understand Global Change and to Benefit Society: Science and User Needs. Deutsche Geodatische Kommission der Bayerischen Akademie der Wissenschaften, Reihe B, Angewandte Geodesie, Heft Nr. 320, 1–124.

Pail R, Bingham R, Braitenberg C, Dobslaw H, Eicker A, Guntner A, Horwath M, Ivins E, Longuevergne L, Panet I, Wouters B, IUGG Expert Panel (2015b) Science and User Needs for Observing Global Mass Transport to Understand Global Change and to Benefit Society. Surveys in Geophysics, 36(6), 743–772, DOI: 10.1007/s10712-015-9348-9.

Pail R, Bamber J, Biancale R, Bingham R, Braitenberg C, Cazenave A, Eicker A, Flechtner F, Gruber T, Güntner A, Heinzel G, Horwath M, Longuevergne L, Müller J, Panet I, Savenije H, Seneviratne S, Sneeuw N, van Dam T,

Wouters B (2019) Mass variation observing system by high low inter satellite links (MOBILE) – a new concept for sustained observation of mass transport from space. Journal of Geodetic Science, under review.

Panet I, Flury J, Biancale R, Gruber T, Johannessen J, van den Broeke MR, van Dam T, Gegout P, Hughes CW, Ramillien G, Sasgen I, Seoane L, Thomas M (2013) Earth System Mass Transport Mission (e.motion): A Concept for Future Earth Gravity Field Measurements from Space. Surveys in Geophysics 34(2):141–163, DOI: 10.1007/s10712-012-9209-8.

Papoulis A (1984) Probability, Random Variables, and Stochastic Processes. Front Cover. McGraw-Hill– Mathematics.

Pfeffer WT, Arendt AA, Bliss A, Bolch T, Cogley JG, Gardner AS, Hagen JO, Hock R, Kaser G, Kienholz C, Miles ES, Moholdt G, Molg N, Paul F, Radic V, Rastner P, Raup B, Rich J, Sharp M (2014) The Randolph Glacier Inventory: a globally complete inventory of glaciers. Journal of Glaciology, 60, 537–552, DOI: 10.3189/2014JoG13J176

Reguzzoni M (2003) From the time-wise to space-wise GOCE observables. Advances in Geosciences, 1, 137–142.

Reguzzoni M, Tselfes N (2009) Optimal multi-step collocation: application to the space- wise approach for GOCE data analysis. Journal of Geodesy, 83(1), 13–29, DOI: 10.1007/s00190-008-0225-x.

Reguzzoni M, Gatti A, De Gaetani CI, Migliaccio F, Sansò F (2014) Locally adapted space-wise grids from GOCE data. Geophysical Research Abstracts Vol. 16, EGU2014-14010, 2014 EGU General Assembly 2014.

Rodell M, Houser PR, Jambor U, Gottschalck J, Mitchell K, Meng CJ, Arsenaul K, Cosgrove B, Radakovich J, Bosilovich M, Entin JK, Walker JP, Lohmann D, Toll D (2004) The Global Land Data Assimilation System. Bulletin of the American Meteorological Society, 85, 381–394, DOI: 10.1175/BAMS-85-3-381.

Rosi G, Sorrentino F, Cacciapuoti L, Prevedelli M, Tino GM (2014) Precision measurement of the Newtonian gravitational constant using cold atoms. Nature, 510, 518521.

Roura A (2017) Circumventing Heisenberg's Uncertainty Principle in Atom Interferometry Tests of the Equivalence Principle. Physical Review Letters, 118, 160401.

Sneeuw N, van Gelderen M (1997) The polar gap. In: Sansó F, Rummel R (eds) Geodetic Boundary Value Problems in View of the One Centimeter Geoid. Lecture Notes in Earth Sciences, vol. 65. Springer, Berlin, Heidelberg.

Sorrentino F, Bertoldi A, Bodart Q, Cacciapuoti L, de Angelis M, Lien Y, Prevedelli M, Rosi G, Tino GM (2012) Simultaneous measurement of gravity acceleration and gravity gradient with an atom interferometer, Applied Physics Letters 101, 114106.

Sorrentino F. Bodart Q, Cacciapuoti L, Lien YH, Prevedelli M, Rosi G, Salvi L. Tino GM (2014) Physical Review A, 89, 023607.

Tapley B, Reigber C (2001) The GRACE mission: status and future plans. EOS Transactions American Geophysical Union, 82(47), Fall Meet. Suppl., Abstract G41C-02.

Tino GM, Sorrentino F, Aguilera D, Battelier B, Bertoldi A, Bodart Q, Bongs K, Bouyer P, Braxmaier C, Cacciapuoti L, Gaaloul N, Gurlebeck N, Hauth M, Herrmann S, Krutzik M, Kubelka A, Landragin A, Milke A, Peters A, Rasel EM, Rocco E, Schubert C, Schuldt T, Sengstock K, Wicht A (2013) Precision Gravity Tests with Atom Interferometry in Space. Nuclear Physics B - Proceedings Supplements, 243–244, 203–217.

Tino GM and Kasevich MA, Eds. (2014) Atom interferometry: proceedings of the International School of Physics "Enrico Fermi", Course 188, Varenna on Lake Como, Villa Monastero, 15-20 July 2013, IOS Press and Società Italiana di Fisica.

Uieda L, Barbosa VCF, Braitenberg C (2016) Tesseroids: forward modeling gravitational fields in spherical coordinates. Geophysics, 81(5), F41–F48, DOI: 10.1190/GEO2015-0204.1.

Wessel P, Sandwell DT, Kim SS (2010) The global seamount census. Oceanography, 23(1), 24–33. DOI: 10.5670/oceanog.2010.60.

Yi S, Freymueller JT, Sun W (2016) How fast is the middle-lower crust flowing in eastern Tibet? A constraint from geodetic observations. Journal of Geophysical Research, 121, 6903–6915, DOI: 10.1002/2016JB013151.